COMMUNICATIONS IN COMPUTATIONAL PHYSICS
Vol. **2**, No. 3, pp. 477-500

Commun. Comput. Phys.
June 2007

A Numerical Comparison of Outflow Boundary Conditions for Spectral Element Simulations of Incompressible Flows

Chuanju Xu* and Yumin Lin

School of Mathematical Sciences, Xiamen University, Xiamen 361005, China.

Received 21 July 2006; Accepted (in revised version) 25 September, 2006

Communicated by Jie Shen

Available online 31 October 2006

Abstract. Outflow boundary conditions (OBCs) are investigated for calculation of incompressible flows by spectral element methods. Several OBCs, including essential-type, natural-type, periodic-type and advection-type, are compared by carrying out a series of numerical experiments. Especially, a simplified form of the so-called Orlanski's OBCs is proposed in the context of spectral element methods, for which a new treatment technique is used. The purpose of this paper is to find stable low-reflective OBCs, suitable and flexible for use of spectral element methods in simulation of incompressible flows in complex geometries. The computation is firstly carried out for a 2D simulation of Poiseuille-Bénard channel flow with Re=10, Ri=150 and Pr=2/3. This flow serves as a useful example to demonstrate the applicability of the proposed OBCs because it exhibits a feature of vortex shedding propagating through the outflow boundary. Then a 3D flow around an obstacle is computed to show the efficiency in the case of more general geometries. Among the tested OBCs, the advection-type OBCs are proven to have better behavior as compared with the others.

AMS subject classifications: 65M70, 74S25, 76M22

Key words: Spectral element methods, outflow boundary conditions, incompressible flows.

1 Introduction

For the numerical solution of channel or external viscous flow problems, we often have to truncate the original unbounded domain into a bounded one in order to make the problems computable. By doing that, we need to introduce appropriate artificial boundary conditions (ABCs) on the artificial external boundary for the closure purpose. The

*Corresponding author. *Email addresses:* cjxu@xmu.edu.cn (C. Xu), lym@xmu.edu.cn (Y. Lin)

ABCs must meet a fundamental requirement: a unique solution inside the finite computational domain exists and can be computed within the desired accuracy as compared to the original solution given by the infinite domain problem.

This paper is focused on outflow ABCs (OBCs), which are critical in many flow simulations. It has been observed that unsuitable OBCs may result in undesired artificial boundary layer, which furthermore render the calculation unstable. On the other hand, the construction of the exact OBCs is generally very difficult. There exists much work concerning numerical and theoretical investigations on the OBCs, mainly done in the framework of finite difference and finite element methods, see for example [2, 11, 16, 25, 29, 30, 34]. In [26], five OBCs are compared in the framework of finite volume methods. Roughly speaking, these OBCs can be classified into three categories: essential-type, natural-type and Orlanski's type [27]. Similar to many other investigations [1, 17, 27], the numerical experiments presented in [26] show that the OBC of the Orlanski's type is a low-reflective boundary condition. We refer to [1, 36] for a review of OBCs for elliptic flows.

The aim of this paper is to compare several OBCs for the computation of certain unsteady channel or external flows by using spectral element methods. The tested OBCs include the traditional boundary condition of essential-type and natural-type, as well as of advection-type (a simplified form of the so-called Orlanski's boundary condition). The use of the latter is based on an essential assumption saying that the Navier-Stokes equations can be linearized in the far field against the free-stream background. We will check the behavior of the advection-type OBCs by discussing its implementation method and accuracy in the context of spectral element methods. It is known that the choice of OBCs is related to the numerical method used in the simulation. Different methods treat the boundary conditions in different manners. In other words, the boundary conditions suitable for the finite difference method are not necessarily applicable to the finite element or spectral methods. Generally, low-order methods, like finite difference methods, treat the boundary conditions in a more arbitrary way as compared to the high order methods, like spectral methods. The latter is heavily based on the variational formulation, and requires global integration of the boundary conditions into the uniform formulation. It is well-known that when the solution of the problem is sufficiently smooth, the convergence of the spectral method is exponential. However, to keep this convergence rate, the treatment of the boundary conditions must be as accurate as the spectral approximation.

In this paper, we restrict ourselves to the following OBCs: 1) periodic conditions; 2) essential OBCs; 3) natural OBCs, $\frac{\partial \varphi}{\partial n}=0$; 4) advection OBCs, $\frac{\partial \varphi}{\partial t}+V\frac{\partial \varphi}{\partial n}=0$. In the above expressions, φ stands for the related variables (mostly, the velocities or temperature), V is a vector to be determined, n is the outward normal on the outflow boundary (hereafter we use letters of boldface type to denote vectors and vector functions). Among these OBCs, only the essential one is a standard boundary condition for spectral element approximations to the Navier-Stokes equations; the others have to be modified or transformed before application. Especially, we will propose an implementation technique to deal with the advection OBCs in the framework of spectral element methods. For com-

parison, we will also present the results from the periodic OBCs. Part of the results has been previously reported in [39], but the numerical method used here and the 3D simulation results are new. We mention in passing that in the framework of spectral collocation methods, a similar technique, combined with the local low order interpolation, has been proposed in [9,10]. However for spectral element approximations, it is highly desirable to transform the advection condition into an essential one, as will be shown in this paper.

The numerical experiments will be firstly carried out for a 2D simulation of Poiseuille-Bénard channel flow, with Re=10, Ri=150 and Pr=2/3, for which numerous experimental results exist [7, 20, 28, 30, 35], making the comparison possible. Then a 3D flow around an obstacle is computed to show that the proposed implementation techniques can be realized in more general geometries.

The outline of this paper is as follows. In Section 2, we present the governing equations and describe the numerical methods. The treatment details of the advection OBCs for spectral element methods will be given. In Section 3, an efficient iteration method is presented. The numerical experiments are carried out in Section 4, where we make comparisons for various OBCs. The conclusion is given in Section 5.

2 Governing equations and numerical methods

2.1 Governing equations

The flow of an incompressible fluid is governed by the following Navier-Stokes equations:

$$\begin{cases} \dfrac{\partial \boldsymbol{u}}{\partial t} - \dfrac{1}{Re}\Delta \boldsymbol{u} + (\boldsymbol{u}\cdot\nabla)\boldsymbol{u} + \nabla p = \boldsymbol{f} & \text{in } \Omega \ \text{(Momentum equation)}, \\ \nabla\cdot\boldsymbol{u} = 0 & \text{in } \Omega \ \text{(Continuity equation)}, \end{cases} \tag{2.1}$$

where $\boldsymbol{u} := (u_1, \cdots, u_d)$, $d \le 3$, and p are respectively the adimensioned velocity and pressure, $\boldsymbol{f}$ is the forcing term, $\Omega \subset \mathbb{R}^d$ is the computational domain. The characteristic scales for the velocity and pressure are respectively mean velocity U_0 and $\rho_0 U_0^2$, where ρ_0 is the density. Re is the Reynolds number, based on the characteristic length, mean velocity U_0, and the kinematic viscosity ν. There are many computational issues that arise from working with these equations. One of these issues is related to boundary conditions: if the computational domain is bounded, then appropriate boundary conditions must be specified in order for the problem to have a unique solution.

For the Poiseuille-Bénard flow, additional to the momentum and continuity equations (2.1), the governing equations also include an energy equation. More precisely, if assume the Boussinesq approach holds, then we have

$$\begin{cases} \dfrac{\partial \boldsymbol{u}}{\partial t} - \dfrac{1}{Re}\Delta \boldsymbol{u} + (\boldsymbol{u}\cdot\nabla)\boldsymbol{u} + \nabla p = Ri\ T\boldsymbol{k} & \text{in } \Omega, \\ \nabla\cdot\boldsymbol{u} = 0 & \text{in } \Omega, \\ \dfrac{\partial T}{\partial t} + (\boldsymbol{u}\cdot\nabla)T - \dfrac{1}{Re\ Pr}\Delta T = 0 & \text{in } \Omega \ \text{(energy equation)}, \end{cases} \tag{2.2}$$

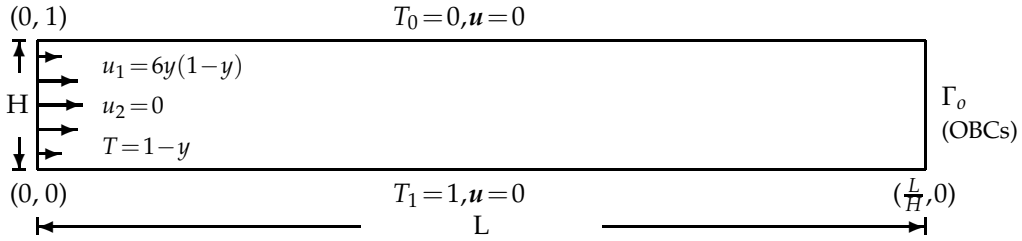

Figure 1: Domain configuration for the Poiseuille Bénard flow.

where T is the adimensioned temperature. The characteristic scale for the temperature is the temperature difference between the top side and bottom side T_1-T_0. The spatial and temporal variables are respectively scaled by the channel height H and the ratio H/U_0. $Ri:=g\beta(T_1-T_0)H/U_0^2$ is the Richardson number, $Pr:=\nu/k$ is the Prandtl number, with β,k and g are respectively heat expansion, thermodiffusion and gravity coefficients, and $\boldsymbol{k}$ is the usual unit vertical vector.

The computational domain and the boundary conditions are shown in Fig. 1. The initial conditions are

$$u_1(x,y,0)=6y(1-y), \quad u_2(x,y,0)=0, \quad T(x,y,0)=1-y+\varepsilon,$$

where ε is the temperature perturbation parameter. The perturbation amplitude needed to provoke the thermodynamic instability depends on the problem configuration, such as domain size, mesh size, adimensioned parameters Re,Ri and Pr etc. In all calculations performed in this paper, we use $\varepsilon=10^{-2}$.

The simulations of the 3D flow past an obstacle are carried out in a domain similar to the one given in Fig. 2, with one periodic direction (z-periodic direction). In this figure a spectral element mesh on a $xy-$plane is particularly shown, and the outflow boundary is the face marked by "OBCs". The approximation in the z-periodic direction makes use of a Fourier method.

2.2 Boundary conditions on the outflow boundary

Let $\partial\Omega=\Gamma_D\cup\Gamma_N$, where Γ_D stands for the part of boundary on which we impose the essential boundary conditions, Γ_N denotes the natural boundary, which may be empty. We compare the following four types of OBC on Γ_o:

1) OBC1 (only for the configuration of Fig. 1): periodicity, $\boldsymbol{u}(L,y,t)=\boldsymbol{u}(0,y,t)$, $T(L,y,t)=T(0,y,t)$. In this case we have $\Gamma_N=\emptyset$. Generally, for the problems with periodic solution, the periodic OBC is adequate: there is no reflection of the outflow boundary, neither of the inflow boundary. Unfortunately, it usually requires anticipated knowledge on the wavelength of the solution in order to correctly set up the computational domain.

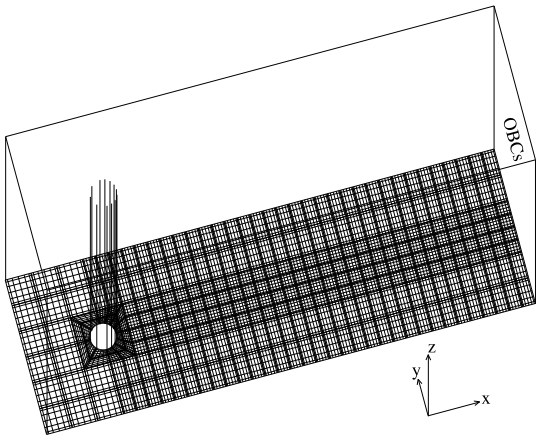

Figure 2: An example of the domain for the 3D flow past the circular cylinder: a spectral element mesh in a $xy-$plane is shown.

2) OBC2: $\boldsymbol{u}=\boldsymbol{u}^0$, $T=T^0$, where $\boldsymbol{u}^0$, T^0 are chosen to be consistent with the initial conditions. For this essential boundary condition we have $\Gamma_N=\emptyset$. On one side, this OBC is a high-reflective artificial boundary condition, tending to create numerical boundary layers and, on the other side, from the point of view of the computational complexity, the essential boundary condition is simpler to implement as compared with the other OBCs. Moreover, it results in a linear system possessing better algebraic properties.

3) OBC3: $\frac{1}{Re}\frac{\partial u_1}{\partial \boldsymbol{n}}-p=0$, $\frac{1}{Re}\frac{\partial u_2}{\partial \boldsymbol{n}}=0$, $\frac{\partial T}{\partial \boldsymbol{n}}=0$, $\Gamma_N=\Gamma_o$. This OBC, so called the natural boundary condition or "open boundary condition" in some of the literature, is imposed in a weak way via the variational formulation. It is generally believed that OBC3 is lower-reflective than OBC2 [36]. A disadvantage of this OBC, as confirmed later by our numerical tests, is that the resulting linear system exhibits worse properties as compared to OBC2.

4) OBC4: $\frac{\partial \boldsymbol{u}}{\partial t}+U_0\frac{\partial \boldsymbol{u}}{\partial n}=0$, $\frac{\partial T}{\partial t}+U_0\frac{\partial T}{\partial n}=0$. This advection condition is a simplified form of the so-called Orlanski's OBCs, which is popular in the finite difference community due to its low-reflective feature [26]. Although a rigorous theoretical foundation is still missing, the justification for use of this OBC is based on the fact that the Navier-Stokes equations can be linearized in the far field against the free-stream background. Our main goal in this paper is to propose an efficient method to employ the OBC4 in the spectral element framework.

2.3 Time discretization

We use the semi-Lagrangian method [6,41], which is a variant of the operator-integration-factor (OIF) splitting technique, to treat the convective terms. In many applications, this method has shown advantage over the classical semi-implicit methods due to the fact

that the OIF method allows for time-step sizes exceeding standard CFL limited time-step sizes.

The semi-Lagrangian temporal discretization results in a saddle point problem coupling the velocity and pressure. To decouple the velocity and pressure, we use an additional splitting step via a matrix factorization. Such an approach was first analyzed and applied to various computations in the papers of Perot [33], Couzy *et al.* [6], and Fischer [8], then generalized by Lin *et al.* [19] to the viscous/inviscid coupled equation. This approach has a common foundation with the traditional projection approaches which lead to a Poisson equation for pressure. Therefore, no boundary conditions are needed for the pressure. More precisely, we use the following second-order time scheme to discretize (2.2)

$$\begin{cases} \dfrac{3\boldsymbol{u}^{n+1}-4\tilde{\boldsymbol{u}}^{n}+\tilde{\boldsymbol{u}}^{n-1}}{2\Delta t}-\dfrac{1}{Re}\Delta\boldsymbol{u}^{n+1}+\nabla p^{n+1}=Ri\,T^{n+1}\boldsymbol{k} & \text{in } \Omega, \\ \nabla\cdot\boldsymbol{u}^{n+1}=0 & \text{in } \Omega, \\ \dfrac{3T^{n+1}-4\tilde{T}^{n}+\tilde{T}^{n-1}}{2\Delta t}-\dfrac{1}{Re\,Pr}\Delta T^{n+1}=0 & \text{in } \Omega, \end{cases} \tag{2.3}$$

where $\triangle t$ is the time step, $\tilde{\boldsymbol{u}}^{n}$, $\tilde{\boldsymbol{u}}^{n-1}$, $\tilde{T}^{n}$ and $\tilde{T}^{n-1}$ are the transports at different instants of the previous solutions on the characteristics. A detailed description of this method was given in [41].

2.4 Spatial discretization and treatment of OBCs

The semi-discretized equations (2.3), subject to appropriate boundary conditions $\boldsymbol{g}$, g_T, φ, and φ_T, can be rewritten into

$$\begin{cases} \alpha\boldsymbol{u}^{n+1}-\dfrac{1}{Re}\Delta\boldsymbol{u}^{n+1}+\nabla p^{n+1}=\boldsymbol{s} & \text{in } \Omega, \\ \nabla\cdot\boldsymbol{u}^{n+1}=0 & \text{in } \Omega, \\ \boldsymbol{u}^{n+1}=\boldsymbol{g} & \text{on } \Gamma_D, \\ B_1\boldsymbol{u}^{n+1}=\varphi & \text{on } \Gamma_N, \\ \alpha T^{n+1}-\dfrac{1}{Re\,Pr}\Delta T^{n+1}=s_T & \text{in } \Omega, \\ T^{n+1}=g_T & \text{on } \Gamma_D, \\ B_2T^{n+1}=\varphi_T & \text{on } \Gamma_N, \end{cases} \tag{2.4}$$

where $\alpha=\frac{3}{2\Delta t}$, $\boldsymbol{s}$, s_T are the source terms, $B_i, i=1,2$, are suitable boundary operators.

The starting point of the spectral element method to the problem (2.4) is to consider its variational formulation (for the sake of simplification, we omit for the moment the time step superscripts and only consider the equations for the velocity and pressure): find $\boldsymbol{u}\in H^1(\Omega)^d$, $p\in L^2(\Omega)$, $\boldsymbol{u}|_{\Gamma_D}=\boldsymbol{g}$, such that

$$\begin{cases} \alpha(\boldsymbol{u},\boldsymbol{v})+\dfrac{1}{Re}(\nabla\boldsymbol{u},\nabla\boldsymbol{v})-(p,\nabla\cdot\boldsymbol{v})=(\boldsymbol{s},\boldsymbol{v}), & \forall\boldsymbol{v}\in V, \\ (\nabla\cdot\boldsymbol{u},q)=0, & \forall q\in L^2(\Omega), \end{cases} \tag{2.5}$$

where $V=\{\boldsymbol{v}\in H^1(\Omega)^d,\boldsymbol{v}|_{\Gamma_D}=0\}$, $(\cdot,\cdot)$ stands for the standard inner product of $L^2(\Omega)$. Here we assume that the boundary condition φ has been incorporated into the source term in the right hand side.

Remark 2.1. When $\Gamma_D=\partial\Omega$ or in the case of periodic boundary condition, an additional condition is necessary to uniquely determine the pressure. We use the condition $\int_\Omega p\,dxdy=0$ in this paper.

In the spectral element discretization, the computational domain is first broken into a number of geometrically conforming macro-elements:

$$\bar{\Omega}=\cup_{k=1}^{K}\bar{\Omega}^k,\quad \text{and}\quad \Omega^k\cap\Omega^l=\emptyset\,,\quad \forall k,l,k\neq l. \tag{2.6}$$

Then piecewise (high order) polynomials are used to approximate the variables. The standard spectral element approximation to problem (2.5), so-called $P_N\times P_{N-2}$ method, reads: find $\boldsymbol{u}_N\in H^1(\Omega)^d\cap P_{N,K}(\Omega)^d, p_N\in P_{N-2,K}(\Omega)$, $\boldsymbol{u}_N|_{\Gamma_D}=I_N\boldsymbol{g}$, such that

$$\begin{cases} \alpha(\boldsymbol{u}_N,\boldsymbol{v}_N)+\dfrac{1}{Re}(\nabla\boldsymbol{u}_N,\nabla\boldsymbol{v}_N)-(p_N,\nabla\cdot\boldsymbol{v}_N)=(\boldsymbol{s},\boldsymbol{v}_N), & \forall\boldsymbol{v}_N\in V_N,\\ (\nabla\cdot\boldsymbol{u}_N,q_N)=0, & \forall q_N\in P_{N-2,K}(\Omega), \end{cases} \tag{2.7}$$

where I_N is an interpolation operator into an appropriate piecewise polynomial space, and

$$V_N=V\cap P_{N,K}(\Omega)^d,$$

with

$$P_{N,K}(\Omega)=\{v\in L^2(\Omega);\ v|_{\Omega^k}\circ\boldsymbol{f}^k\in P_N(\Lambda^2),1\leq k\leq K\}.$$

Here $\boldsymbol{f}^k$ is the transformation function from the reference domain Λ^2, with $\Lambda=(-1,1)$, to Ω^k and P_N is the space of the polynomials of degree not exceeding N.

In the implementation, all the integrals are evaluated by using the Legendre Gauss-Lobatto quadrature [3, 32]. This is for the following reasons. First, the exact evaluation of the integrals is expensive if general basis functions are used. We may try to construct a particular orthogonal basis in order to reduce the evaluation cost. However, this idea seems impractical for problems with variable coefficients and/or in complex geometries. Second, for the spectral element method, it has been shown that using the Gauss-Lobatto quadrature rule together with the Lagrangian basis one can efficiently and accurately calculate the integral of a polynomial function.

According to the formulation (2.7), the discrete velocity and temperature are computed in the Legendre-Gauss-Lobatto points, defined by the tensor product of the zeros of $(1-x^2)L_N'(x)$ in $[-1,1]$. The pressure is computed in the Legendre-Gauss points based on the zeros of $L_N(x)$ in $[-1,1]$. There are $(N+1)^{d-1}$ velocity and temperature points in the edge (face in 3D case) of two joint elements, hence the continuity of the velocity and temperature on the elemental interfaces are naturally imposed. It is worthwhile to note that the pressure is not required to be continuous across the interfaces between the macro-elements.

Treatment of the outflow boundary conditions

Without loss of generality we only consider the equations for the velocity and pressure:

1) OBC1: Periodicity on the input and output boundaries can be regarded as the continuity of the velocity field at the periodic boundary pair. In fact, in our code the periodic boundaries are treated as fictitious elemental interfaces. We emphasize that in the periodic case, the flow is no longer driven by the specified mean velocity, but via appropriate forcing such that the flow-rate attains the correct value depending on the Reynolds number (see e.g. [12] for details).
2) For OBC2, we have $\Gamma_D=\partial\Omega$, hence the outflow boundary conditions are imposed by simply specifying the velocity on the corresponding Gauss-Lobatto collocation points.
3) In the case of OBC3, $\Gamma_D=\partial\Omega\backslash\Gamma_o$, the outflow boundary conditions are implicitly imposed in the variational formulation.
4) For OBC4, we introduce the following implementation method: once the velocity at time step n is obtained, we solve the transport equation

$$\frac{\partial \boldsymbol{u}}{\partial t}+U_0\frac{\partial \boldsymbol{u}}{\partial \boldsymbol{n}}=0 \tag{2.8}$$

to determine the condition on the outflow boundary at time step $t^{n+1}=(n+1)\Delta t$. In fact, if $\boldsymbol{u}$ is known at t^n, then the exact expression of $\boldsymbol{u}$ at t^{n+1} is: $\boldsymbol{u}(\boldsymbol{x},t^{n+1})=\boldsymbol{u}(\boldsymbol{x}-U_0\cdot\boldsymbol{n}\Delta t,t^n)$. This implies that the value of the velocity at a mesh point on the outflow boundaries at t^{n+1} is equal to the value of $\boldsymbol{u}$ at the corresponding characteristics foot at t^n. In Fig. 3(a) we show the schematic diagram, where the four outflow elements are plotted. In this figure, the mesh nodes on the outflow boundary and the corresponding characteristic feet are respectively marked by $\circ$ and $\bullet$. In our domain configuration, we have $U_0=(u_1^0,0)$, i.e., the vertical component of the mean velocity vanishes, hence

$$\boldsymbol{u}(x,y,t^{n+1})=\boldsymbol{u}(x-u_1^0\Delta t,y,t^n).$$

As a result, each outflow boundary node and its characteristic foot lie on a line parallel to the x-axis, so that the value of $\boldsymbol{u}(\boldsymbol{x}-U_0\cdot\boldsymbol{n}\Delta t,t^n)$ at each node can be easily obtained by an one-dimensional interpolation based on the elemental Gauss-Lobatto points lying on this line. In fact, in many applications we can construct a spectral element mesh with OBCs elements meeting this requirement. Otherwise, in more general cases two-dimensional interpolations based on all elemental Gauss-Lobatto points will be needed to evaluate $\boldsymbol{u}(\boldsymbol{x}-U_0\cdot\boldsymbol{n}\Delta t,t^n)$; see Fig. 3(b) for such a case. In summary, OBC4 can be treated as an essential outflow boundary condition, but with the velocity and temperature on the outflow boundary updated at each time step.

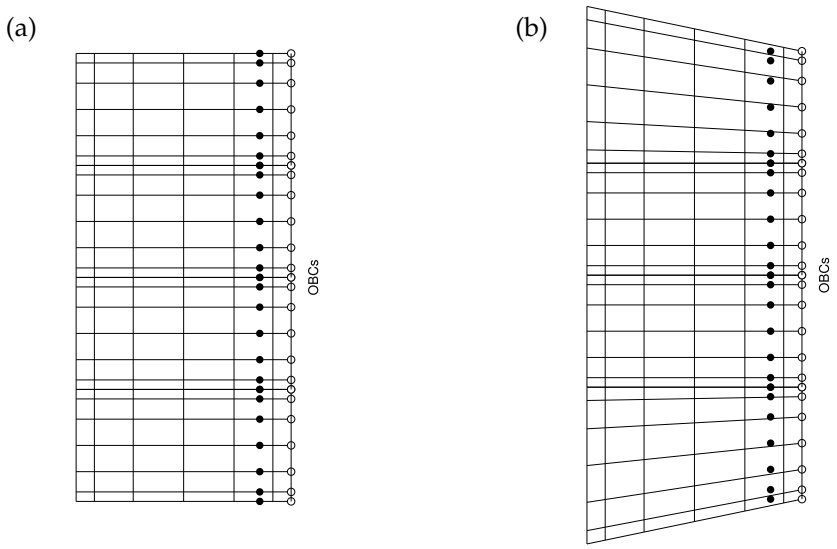

Figure 3: Locations of the characteristic feet (•) stemming from the outflow boundary nodes (○). (a): Only need 1D interpolation; (b): Need 2D interpolation.

3 Uzawa algorithm and matrix factorization

We first express $\boldsymbol{u}_N$ in terms of the Lagrangian interpolants associated with the Gauss-Lobatto points, p_N in terms of the Lagrangian interpolants associated with the Gauss points. Then we choose each test function $\boldsymbol{v}_N$ and q_N to be nonzero at only one global collocation point. Using the Gauss-Lobatto and Gauss quadrature formulas respectively to the velocity and pressure term in (2.7), we arrive at the following matrix statement:

$$\begin{cases} H\underline{u}_i - G_i\underline{p} = B\underline{s}_i\,, \ i=1,2, \\ -D_i\underline{u}_i = \underline{0}\,, \\ H_T\underline{T} = B\underline{s}_T\,, \end{cases} \tag{3.1}$$

where the underlined letters denote vectors of the nodal values, $\boldsymbol{G} := (G_1, G_2)^T$ is the discrete gradient matrix, $\boldsymbol{D} := (D_1, D_2)$ the discrete divergence matrix, B the mass matrix, H and H_T the Helmholtz matrices defined respectively by

$$H = \alpha B + \frac{1}{Re}A, \quad H_T = \alpha B + \frac{1}{Re\,Pr}A, \tag{3.2}$$

with A the discrete Laplacian matrix.

The classical Uzawa algorithm consists of decoupling the original $(\underline{u}_i, \underline{p})$ saddle problem in (3.1) into two positive definite symmetric systems [21, 22]:

$$(D_i H^{-1} G_i)\underline{p} = -D_i H^{-1} B\underline{s}_i\,, \tag{3.3}$$

$$H\underline{u}_i = G_i\underline{p} + B\underline{s}_i\,, \quad i=1,2. \tag{3.4}$$

The advantage of this procedure is that the pressure and velocity are completely decoupled in the solution process. The apparent disadvantage is that the system in the discrete pressure involves the inverse H^{-1}, which usually necessitates an inner iterative solver. Indeed, our numerical experiments have shown that it is computationally expensive to reach the convergence of the outer conjugate gradient iteration [19].

To overcome this difficulty, we use a matrix factorization technique [6, 8, 19, 33, 40] to recast the first two equations of (3.1):

$$\begin{pmatrix} H & 0 & -H\alpha^{-1}B^{-1}G_1 \\ 0 & H & -H\alpha^{-1}B^{-1}G_2 \\ -D_1 & -D_2 & 0 \end{pmatrix} \begin{pmatrix} \underline{u}_1 \\ \underline{u}_2 \\ \delta\underline{p} \end{pmatrix} = \begin{pmatrix} B\underline{s}_1+G_1\underline{p}^n \\ B\underline{s}_2+G_2\underline{p}^n \\ \underline{0} \end{pmatrix} + \begin{pmatrix} \underline{r}_1 \\ \underline{r}_2 \\ \underline{0} \end{pmatrix}, \tag{3.5}$$

where $\underline{p}^n$ is the pressure calculated at the previous time step n. Consequently, $\underline{p}-\underline{p}^n$ is indeed the pressure increment between the current time step $n+1$ and time step n, which will be denoted by $\delta\underline{p}$ hereafter. The residual $\underline{r}_i$ takes the form:

$$\underline{r}_i=(I-H\alpha^{-1}B^{-1})G_i\delta\underline{p}, \quad i=1,2.$$

Neglecting $\underline{r}_i$ in (3.5) and rewriting the resulting system in compact form give:

$$\begin{cases} H\underline{u}_i-(H\alpha^{-1}B^{-1}G_i)(\underline{p}-\underline{p}^n)=B\underline{s}_i+G_i\underline{p}^n, \\ -D_i\underline{u}_i=\underline{0}\,. \end{cases} \tag{3.6}$$

Formally, this method is of second-order accuracy in time, which can be observed by rewriting the residual in the form:

$$\underline{r}_i=(I-H\alpha^{-1}B^{-1})G_i\delta\underline{p}=-\frac{\alpha^{-1}}{Re}AB^{-1}G_i\delta\underline{p}=\mathcal{O}(\Delta t^2),$$

where we have taken into account the fact that $\alpha^{-1}=\mathcal{O}(\Delta t)$ and $\delta\underline{p}=\mathcal{O}(\Delta t)$. Since there is a factor of Δt^{-1} in front of the velocity in (3.5), the local truncation error incurred by neglecting $\underline{\boldsymbol{r}}$ is $\mathcal{O}(\Delta t^3)$. Note that the residual $\underline{\boldsymbol{r}}$ decreases as Re increases. As a result, the error due to the matrix factorization becomes smaller for problems with high Reynolds number.

It is readily seen that the system (3.6) is equivalent to

$$\begin{aligned} &\alpha^{-1}(\boldsymbol{D}B^{-1}\boldsymbol{G})\delta\underline{p}=-\boldsymbol{D}H^{-1}(B\underline{\boldsymbol{s}}+\boldsymbol{G}\underline{p}^n), \\ &H(\underline{\boldsymbol{u}}-\alpha^{-1}B^{-1}\boldsymbol{G}\delta\underline{p})=B\underline{\boldsymbol{s}}+\boldsymbol{G}\underline{p}^n. \end{aligned}$$

As compared to (3.3), the above system on $\delta\underline{p}$ involves only the inverse of a diagonal matrix, B^{-1}, which is much cheaper than the computation of H^{-1}.

Remark 3.1. With OBC2 and OBC4 via the characteristics method, the boundary conditions are purely of essential-type, i.e. $\Gamma_N=\emptyset$. By contrast, OBC3 results in a problem with mixed essential-natural boundary conditions. It is known [4] that in the former cases the resulting linear system shows better algebraic properties as compared to the latter case. This point is confirmed by our numerical experiments.

4 Numerical results

In this section, we will first check the accuracy of the advection OBCs for a selected solution satisfying the exact advection condition. Then the behavior of different OBCs is investigated in detail in terms of the reflection characters near the outflow boundary. For ease of comparison, the numerical experiments are first carried out for a Poiseuille-Bénard flow for which there exists numerous known results. Finally, the flow past an obstacle is simulated to demonstrate the applicability of the advection OBCs in more general geometries.

4.1 Accuracy of the characteristics method

In this subsection we focus on an analytical solution to demonstrate that the interpolation procedure used in the implementation of the advection OBCs is stable and preserves the spectral accuracy. To this end, we consider the Navier-Stokes equations (2.1) in $\Omega := \Lambda^2$ with $\nu = 0.01$, and choose the following solution:

$$\begin{cases} u_1(x,y,t) = \sin(t-x)\sin(y), \\ u_2(x,y,t) = -\cos(t-x)\cos(y), \\ p(x,y,t) = (\cos(2(t-x)) - \cos(2y))/4. \end{cases}$$

We set the outflow boundary $\Gamma_o := \{(1,y); y \in \Lambda\}$. It can be checked that the advection condition (2.8) is rigorously satisfied on Γ_o for this solution. In the accuracy test, the computational domain is partitioned into 2×2 square elements. We successively study the spatial and temporal errors.

In the left of Fig. 4, we plot the velocity and pressure errors in the L^2 norm obtained with the advection OBCs. We have taken the time step small enough, say $\Delta t = 10^{-5}$, in order to make sure that the errors stemming from the temporal resolution is negligible. For comparison, errors from the exact essential OBCs are also plotted. It is observed that there is no significant difference between the two OBCs, and the errors show exponential decay for both OBCs as the polynomial degree is increased. This demonstrates that the interpolation procedure used preserves the so called spectral accuracy. It should be mentioned that the spectral accuracy holds only when the exact solution satisfies the advection condition, which is generally not the case in practical situations.

The right of Fig. 4 shows the errors of the velocity and pressure as functions of the time step Δt, where the temporal convergence rate can be observed. The polynomial degree N is now chosen big enough such that the error is dominated by the time discretization. As expected, the error is of second order for the velocity and more than 3/2-order for the pressure [15]. We point out that if the "open boundary condition (OBC3)" is used, the second-order projection method [13, 14] can only yield 3/2-order accuracy for the velocity and first-order accuracy for the pressure in the L^2 norm. This is an advantage of the advection OBCs against the "open boundary condition" if a projection method is applied for the time discretization.

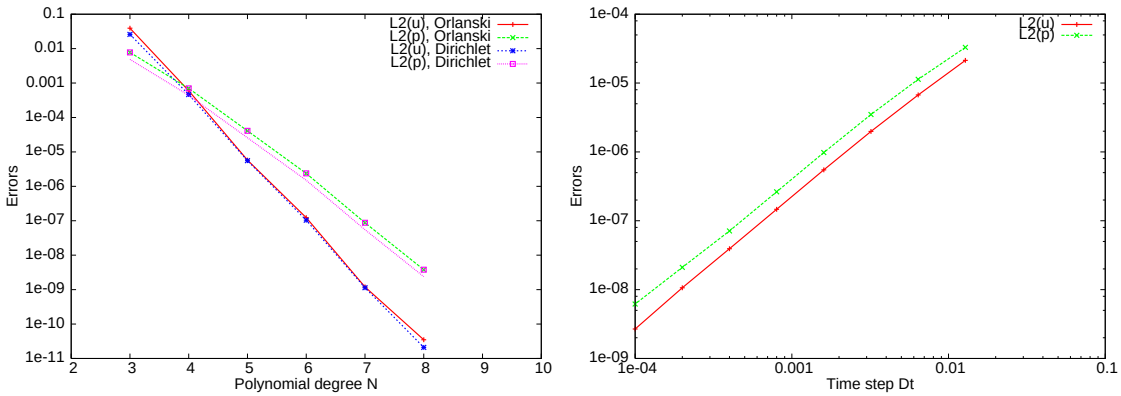

Figure 4: Errors of the velocity and pressure as a function of the polynomial degree (left) and the time step (right).

4.2 Poiseuille-Bénard channel flow

Mesh influence. In order to clearly distinguish different error sources, we first study the influence of the mesh on main physical quantities. To this end we consider OBC1 (periodic OBCs) to minimize the reflection of the OBCs. We take Re=10,Ri=150, and Pr=2/3, for which it is known (see Evans and Paolucci [7]) that the benchmark value of the instability wavelength is $\lambda=1.44$. The domain length is accordingly taken to be $L=k\lambda$, with k a positive constant. In what follows we fix $k=4$, i.e. $L=5.76$, so that 4 convective vortices are expected to appear in the computational domain. In Fig. 5, a typical spectral element mesh, denoted by M48N6, is shown, where there are 48 elements and 7×7 Gauss-Lobatto points in each element (corresponding to polynomial degree $N=6$). For reason of clarification, the pressure nodes, i.e., the Gauss points are not shown. The total node number is 1825 for the velocity and temperature, and 1200 for the pressure. The result from mesh M48N6 is compared to the cases of mesh M48N8, where the polynomial degree is increased to $N=8$ while keeping the element number unchanged, and M96N6, where the element number is doubled by splitting each element into two equal elements while keeping the polynomial degree unchanged.

In Fig. 6, we present the evolution of the horizontal velocity and temperature at a selected point $(2.88,0.5)$ as a function of time. It is observed that the starting times of the thermodynamic instability are different for the three meshes: For the mesh M96N6 the thermodynamic instability and the vortices are created in an earlier time, in contrast to M48N8, where the instability is less sensitive to the perturbation. The difference in the starting time for different meshes may be incurred by the fact that the spatial resolution of the fluctuation scales is important in the formation of the vortex. Regardless of this difference, the asymptotic flow structures from the three meshes are very close. This point can be observed in Fig. 7, in which the isolines of the vorticity at $t=t^*$ are plotted, where t^* is the time when the temperature attains its minimum at point $(2.88,0.5)$ (the minimum is 0.299) during the fifth time period. There is no visible deviation between the

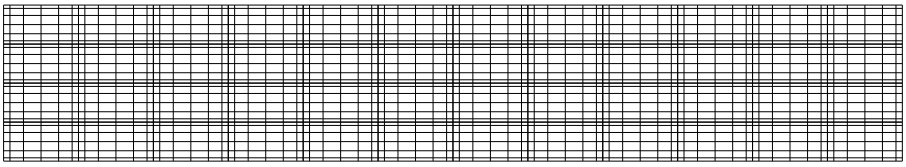

Figure 5: Spectral element mesh M48N6; only Gauss-Lobatto nodes are shown, total node number is 1825.

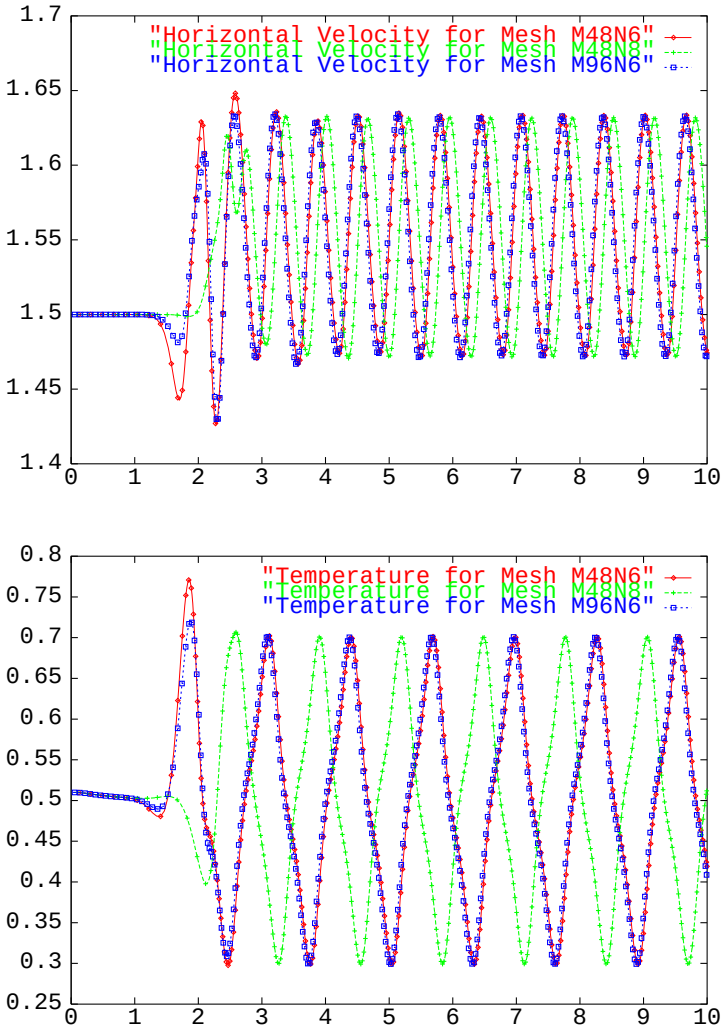

Figure 6: Horizontal velocity (top) and temperature (bottom) at the point $(2.88,0.5)$ as a function of time for meshes M48N6($\diamond$), M48N8($+$) and M96N6($\square$).

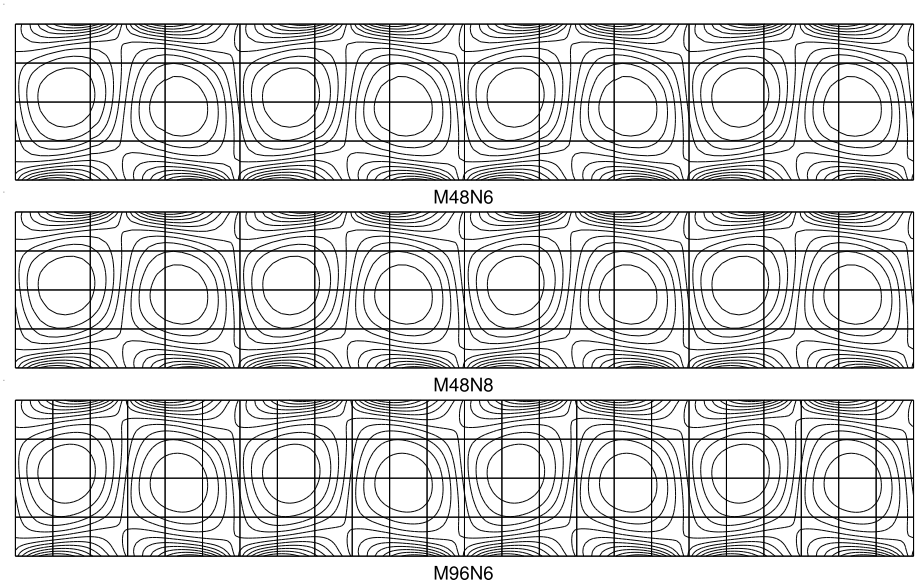

Figure 7: Comparison of the iso-vorticity for different meshes.

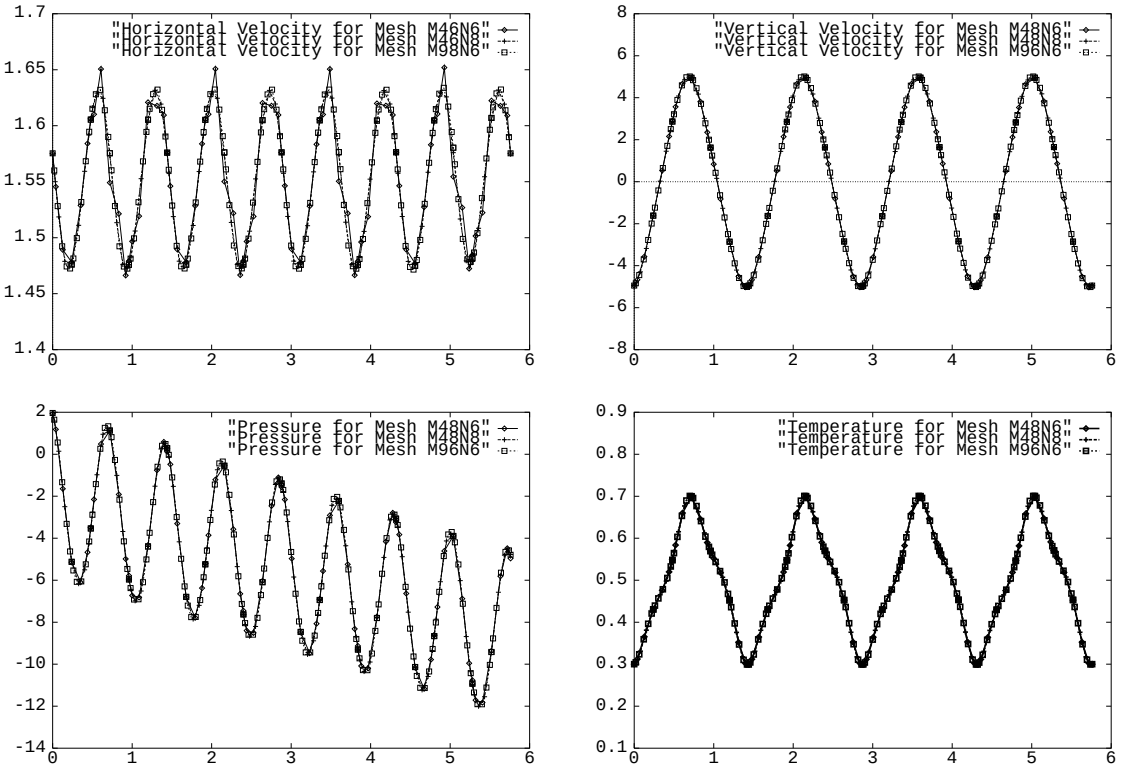

Figure 8: Profiles of the horizontal velocity, vertical velocity, pressure, and temperature along axis y=0.5 at $t=t^*$ obtained respectively by the meshes M48N6($\diamond$), M48N8($+$), and M96N6($\square$).

Table 1: Comparison of the flow characteristic quantities between different meshes and Reference values for $Re=10, Ri=150, Pr=2/3$.

	τ	λ	$u_{1,max}$	$u_{1,min}$	$u_{2,max}$	$u_{2,min}$	ω_{max}	ω_{min}	φ_{max}	φ_{min}
M48N6	1.301	1.440	4.3603	-2.6779	4.9364	-5.0273	28.694	-28.648	1.671	-0.662
M48N8	1.298	1.440	4.3691	-2.6826	4.9558	-5.0214	28.818	-28.736	1.675	-0.674
M96N6	1.300	1.440	4.3572	-2.6806	5.0136	-5.0145	28.821	-28.828	1.669	-0.669
[7]	1.332	1.447	4.3958	-2.7329	5.0319	-5.0587				

results from the three meshes. More precise comparison is made by plotting the profiles on some selected lines. In Fig. 8 we present the distribution of the velocity, pressure and temperature along the axis $y=0.5$ at $t=t^*$. Except of the minor disagreement observed on the vertical velocity (the relative error is less than 3%), the curves for the remaining fields coincide with each other perfectly. Table 1 lists the flow characteristic parameters, where τ is the periodicity length of the flow structure, λ the wavelength, $\boldsymbol{u}_{max}$ and $\boldsymbol{u}_{min}$ are the maximum and minimum of the velocity, respectively, ω and φ the vorticity and stream-function respectively. For reason of comparison, the results from [7] are also included in Table 1. We see from this table that the discrepancy of the flow characteristic parameters among different meshes are less than 1%, while the discrepancy with the reference values in [7] is less than 3%. Assuming this error level acceptable, and since the starting time for the instability has no essential influence on the OBCs, we will use mesh M48N6 in all calculations that follow.

OBCs influence. Now we investigate the behaviors of the OBCs by simulating the Poiseuille-Bénard flow with the same parameters as above. Figs. 9 and 10 show respectively the isolines of the streamfunction and vorticity at $t=t^*$ computed by using various OBCs, where the reference results "Refs" have been obtained from the calculation in a domain of double length (i.e. $L=11.52$) by using OBC4. It is believed that the influence of the OBCs is limited to a region near the outflow boundary, so that the "Refs" results can be thought to be exact. By comparing the flow structures in the neighborhood of the outflow boundary in Figs. 9 and 10, it is seen that only OBC1 (the periodic boundary condition) and OBC4 (the advection condition) give results close to "Refs". On the other hand, the impact of all OBCs in the region far away from the outflow boundary is very small. This is verified in Fig. 11, where the history of the vertical velocity and temperature at $(2.88,0.5)$ as a function of time is plotted. Keeping in mind that t^* was defined as the instant that the temperature attains its minimum at the interior point $(2.88,0.5)$, we see from these figures that, except for the OBC1, there is only slight discrepancy in t^* between the considered OBCs. Moreover, the wave shapes are also in good agreement with each other.

A close comparison is made by looking at some pointwise values. In Fig. 12 we present the profiles of the velocity, pressure and temperature along axis y=0.5. Ignor-

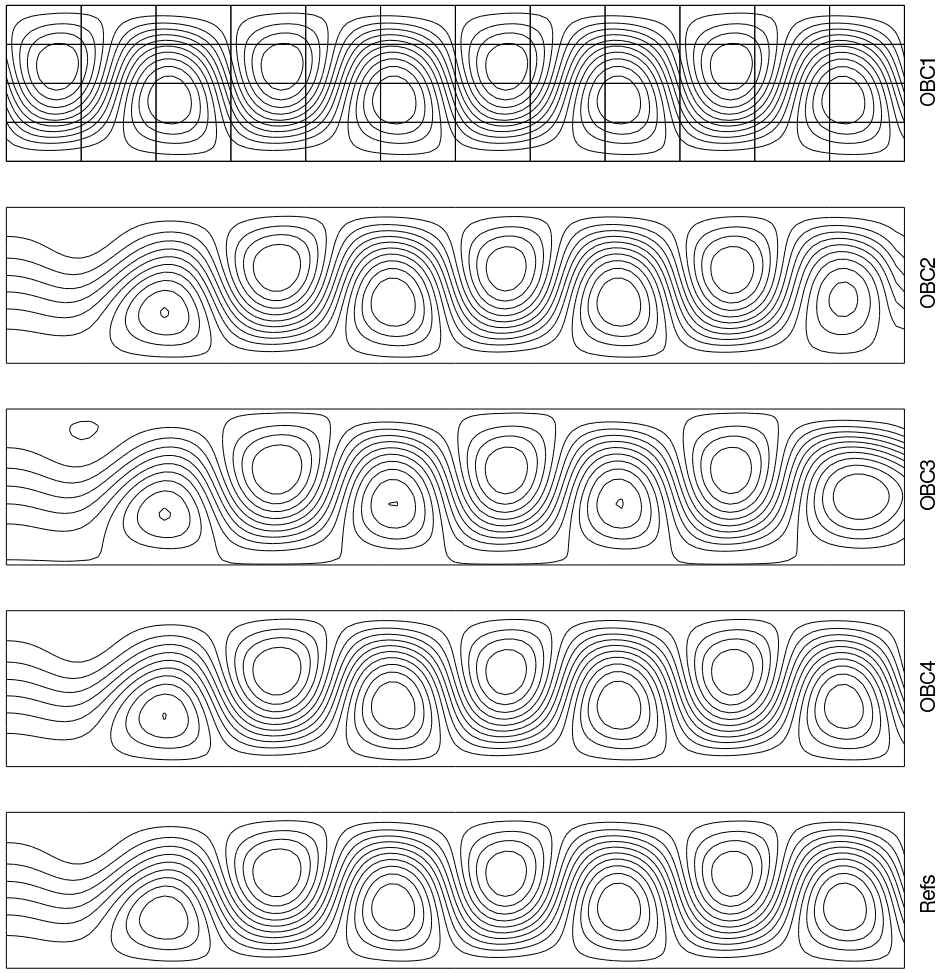

Figure 9: Comparison of the flow structures obtained with various OBCs and with the reference: streamlines.

ing the essential difference in the inflow boundary for the periodic condition, OBC1 and OBC4 are in a much better agreement with Refs than OBC2 and OBC3, especially in the outflow zone. Note that in the pressure figure, the pressure is defined up to a constant. Fig. 13 describes the distribution of the same variables on the outflow boundary: line $x=5.76$. A similar observation can be made: OBC1 and OBC4 lead to much better results as compared to OBC2 and OBC3.

Finally, we list the computed flow characteristic parameters in Table 2; also listed are the results from [7,26] for comparison. Apart from few exceptions (for example $u_{2,min}$ by OBC2), better results are produced again by using OBC1 and OBC4.

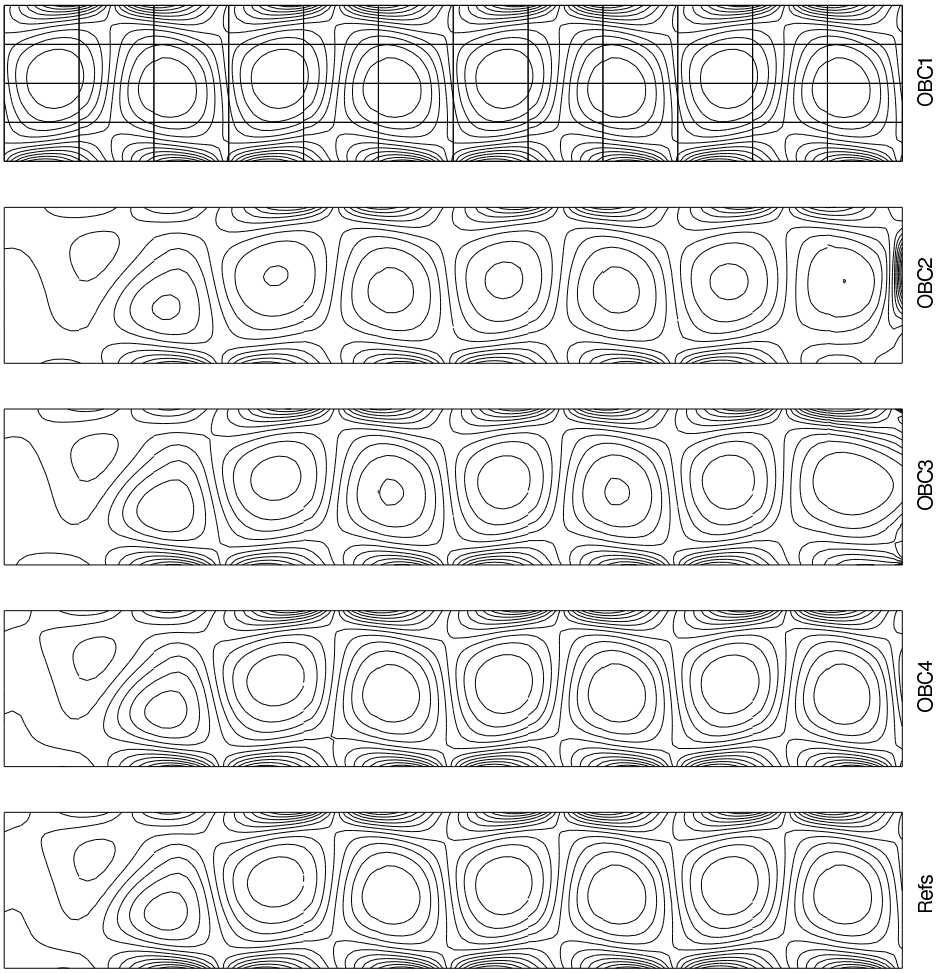

Figure 10: Comparison of the flow structures obtained with various OBCs and with the reference: iso-vorticity.

4.3 3D Flow past a circular cylinder

Flow past a circular cylinder is characterized by the complex wake dynamics, and has been extensively studied by many authors (see, e.g. [42] and references therein), mostly by experimental and analytical approaches. It has also been the subject of many computational investigations, mainly restricted to the 2D case although a few 3D numerical simulations may still be found (see, e.g., [18,24,31,37]).

The aim of our computation is to study the effect of the advection outflow boundary condition in the domain shown in Fig. 2. A cylinder of unit diameter is located in a hexahedral box with the upstream and downstream boundaries located at 3 and 16 diameters, respectively, from the cylinder center. The upper and the lower walls (perpendicular to

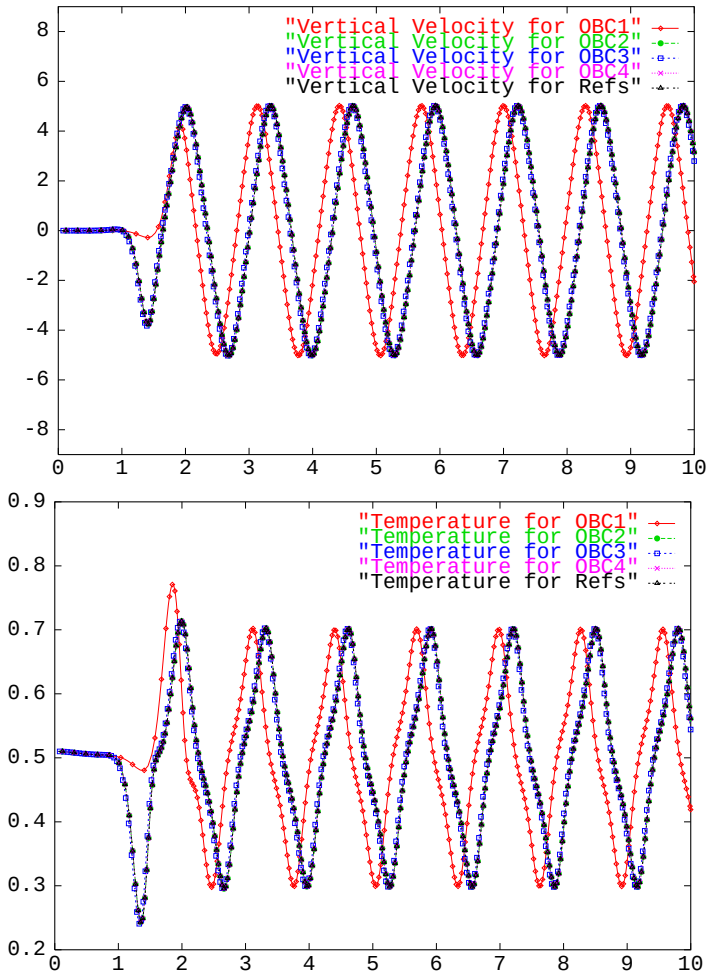

Figure 11: Evolution of the vertical velocity (top) and temperature (bottom) at point $(2.88,0.5)$ as a function of time. The results of OBC2, OBC3 and OBC4 are almost the same.

the y-axis) are located at 3 diameters each from the cylinder. The length of the cylinder is 4 times its diameter. The origin of the axes lies at the center of the cylinder. While the span of the cylinder is aligned with the z-axis, the flow direction is along the x-axis. In the z-direction the periodic condition is assumed, and on all other walls, expect of the OBCs wall, uniform flow velocity is prescribed. A no-slip condition on the velocity is specified on the cylinder wall. At the downstream OBCs boundary, the advection condition for the velocity is applied, which necessitates to solve a 3D transport equation (2.8) by the characteristic method proposed in Section 2.4. The boundary velocity is linearly accelerated from rest until reaching its final speed at $t=1$.

The computation is performed for the flow at $Re=300$. It is known that for Re larger

Table 2: Comparison of the flow characteristic parameters obtained with different OBCs and with Reference values for Re=10, Ri=150, Pr=2/3. ($*$ This parameter is a prefixed value).

	[7]	[26]	OBC1	OBC2	OBC3	OBC4	"Refs"
τ	1.3319	1.296	1.301	1.291	1.299	1.297	1.297
λ	1.4465	1.425	1.440*	1.440	1.443	1.439	1.439
$u_{1,max}$	4.3958	4.072	4.3603	4.5288	5.3192	4.4129	4.3855
$u_{1,min}$	-2.7329	-2.616	-2.6779	-2.8285	-2.8940	-2.8286	-2.8283
$u_{2,max}$	5.0319	4.814	4.9364	4.9232	4.9485	4.9489	4.9662
$u_{2,min}$	-5.0587	-4.909	-5.0273	-5.0587	-5.0374	-5.0977	-5.0189
ω_{max}			28.694	45.386	35.434	28.779	28.867
ω_{min}			-28.648	-29.717	-28.782	-28.860	-28.758
φ_{max}			1.6712	1.6941	1.6893	1.6886	1.6885
φ_{min}			-0.6624	-0.6622	-0.8393	-0.6680	-0.6729

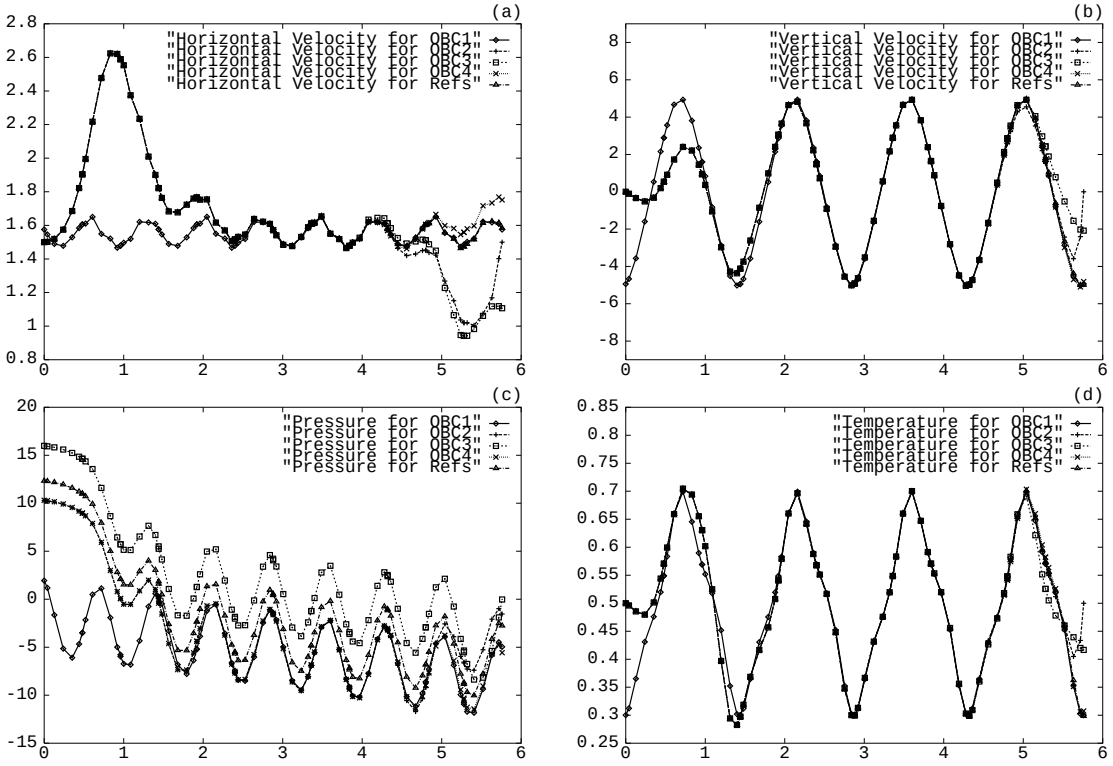

Figure 12: Plot of profiles of the horizontal velocity (a), vertical velocity (b), pressure (c) and temperature (d) along axis y=0.5.

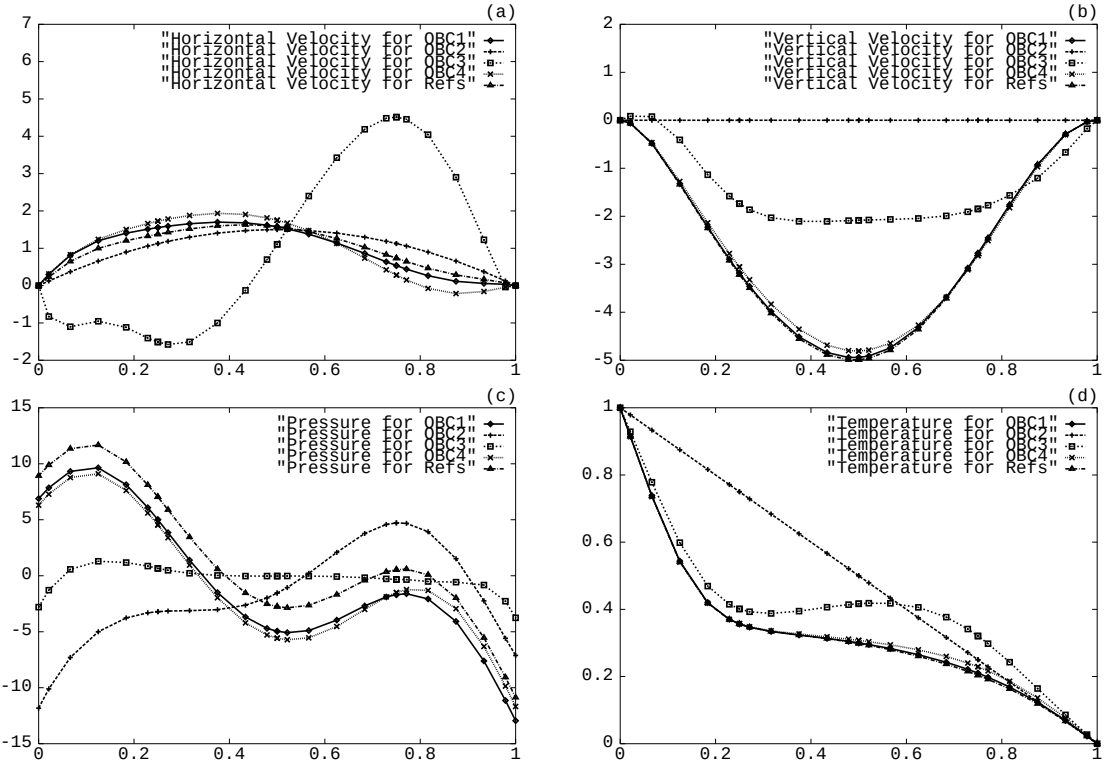

Figure 13: Same as in Fig.12, but at the outlet.

than 180 the wake flow undergoes three-dimensional transitional instabilities. As $Re \approx 260$, the so-called Mode B of vortex shedding occurs [38]. Therefore, the flow with $Re = 300$ is a good example to test the applicability of the advection OBCs.

The spectral element mesh in the xy-plane is shown in Fig. 2. The mesh has 288 elements, each with 6th-order Legendre-Gauss-Lobatto tensor-product basis functions (for the velocity). The Fourier method in the z-direction uses 30 complex Fourier modes, which results in representative 60 xy-planes.

Fig. 14 shows the isosurfaces for the streamwise component of velocity at $t = 60$. The spatial development of the vortex shedding can be observed clearly in the figure. More importantly, the vortex in the region close to the outflow boundary maintains a fair shedding pattern, which implies that the advection boundary condition realizes the correct downstream flow feature. This point is furthermore confirmed in Fig. 15, where we plot the isolines of the streamwise component of velocity at $t=30$ and $t=60$ at two xy-sections: $\{(x,y,z); z = 0\}$ and $\{(x,y,z); z = 0.67\}$. No obvious reflection from the outflow boundary can be observed in the downstream field of these figures.

Note that a full description of the cylinder flow should include the computation of the Strouhal number, the transition from Mode A to Mode B, as well as the vortex dislocations, etc. On the other side, it is found [24] that the flow evolution is sensitive to, besides

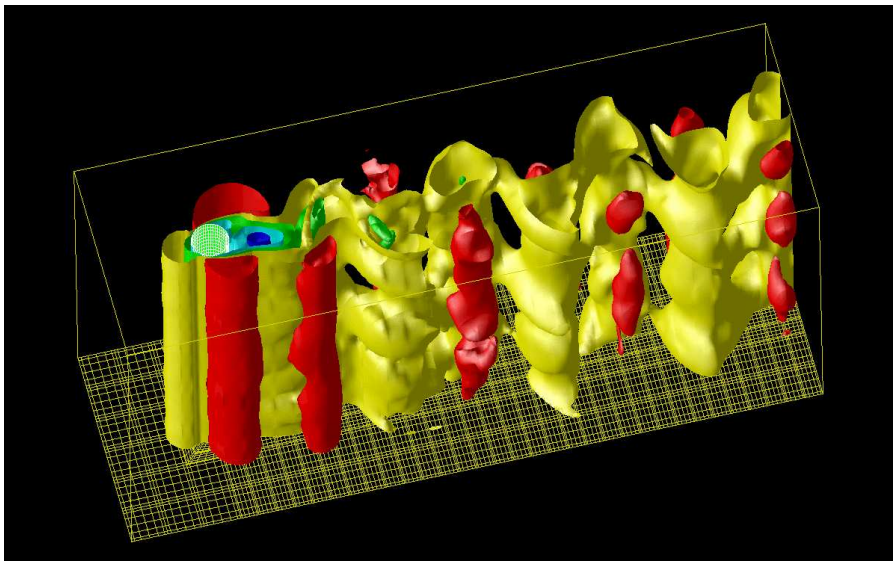

Figure 14: Isosurfaces of the streamwise component of velocity of the 3D cylinder flow at $Re=300$.

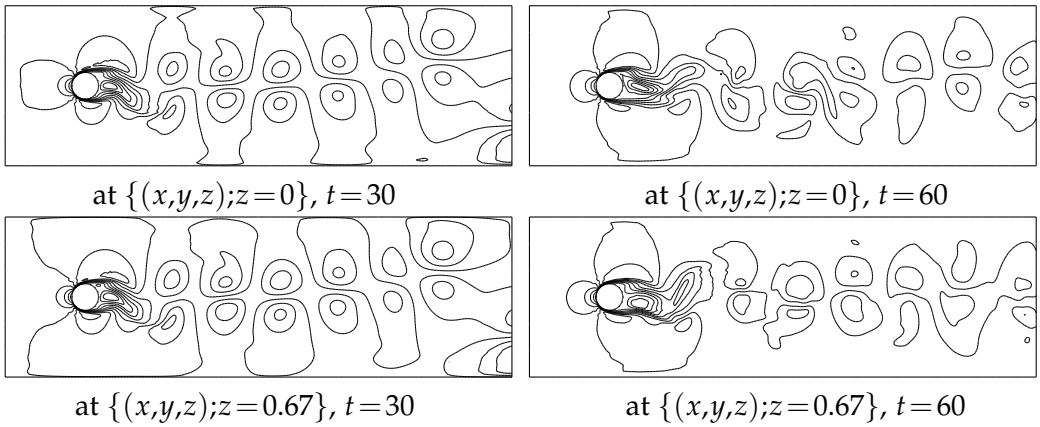

Figure 15: Isolines of the streamwise component of velocity at two xy-sections.

the Reynolds number, various other parameters such as surface roughness, end-effects, aspect ratio, and so on. This makes the numerical comparison difficult. A detailed investigation of the effect of the advection outflow boundary condition on the 3D cylinder flow is beyond the scope of this paper and will be left to a future work.

5 Concluding remarks

A new advection outflow boundary condition has been introduced for spectral element simulations of incompressible flows. This outflow boundary condition takes a simpler

form than most of the other artificial outflow boundary conditions. An implementation technique is detailed in the framework of the spectral element method. As compared to the classical "open boundary condition" (OBC3), the numerical experiments for the Poiseuille-Bénard channel flow and 3D cylinder flow have shown advantages of the advection condition. All our tests suggest that the advection OBC is a low-reflective outflow boundary condition for spectral element simulations for incompressible flows.

One more advantage of using this new outflow boundary condition comes from the fact that the boundary condition of essential-type results in a linear system possessing better properties (smaller condition number) as compared to the natural-type boundary condition [39]. Since, as we have seen in Section 2.4, the advection OBC is treated as an essential outflow boundary condition combined with the characteristic method, the convergence of the iterative method for the resulting algebraic system is faster than that with the "open boundary condition".

Finally, to our knowledge, this is the first spectral element computation of the Poiseuille-Bénard channel flow. Since the spectral method is of high accuracy, we believe that the results obtained from this computation can serve as a benchmark for further investigations.

Acknowledgments

This work was partially supported by NSF China under Grant 10531080, the 973 High Performance Scientific Computation Research Program, and the Program of 985 Innovation Engineering on Information by Xiamen University.

References

[1] A. Bottaro, Note on open boundary conditions for elliptic flows, Numer. Heat Tr. B - Fund., 18 (1990), 243-256.
[2] W. Z. Bao and H. D. Han, Local artificial boundary conditions for the incompressible viscous flow in a slip channel, J. Comput. Math., 15(4) (1997), 335-344.
[3] C. Bernardi and Y. Maday, Approximations Spectrales de Problèmes aux Limites Elliptiques, Springer-Verlag, Paris, 1992.
[4] C. Canuto, M. Y. Hussaini, A. Quarteroni and Z. A. Zang, Spectral Methods in Fluid Dynamics, Springer, New York, Berlin, Heidelberg, London, Paris, Tokyo, 1987.
[5] J. Cahouet and J. P. Chabard, Some fast 3d finite elements solvers for the generalized Stokes problem, Int. J. Numer. Meth. Fluids, 8 (1988), 869-895.
[6] W. Couzy and M. O. Deville, A fast Schur complement method for the spectral element discretization of the incompressible Navier-Stokes equations, J. Comput. Phys., 116 (1995), 135-142.
[7] G. Evans and S. Paolucci, The thermoconvective instability of a plane Poiseuille flow heated from below: a proposed benchmark solution for open boundary flows, Int. J. Numer. Meth. Fluids, 11 (1990), 1001-1013.

[8] P. Fischer, An overlapping Schwarz method for spectral element solution of the incompressible Navier-Stokes equations, J. Comput. Phys., 133 (1997), 84-101.
[9] M. Y. Forestier, R. Pasquetti and R. Peyret, Calculation of 3D wakes in stratified fluids, in the CD of the ECCOMAS 2000 Congress, Barcelona.
[10] M. Y. Forestier, R. Pasquetti, R. Peyret and C. Sabbah, Spatial development of wakes using a spectral multi-domain method, Appl. Numer. Math., 3 (2000), 207-216.
[11] D. F. Griffiths, The 'no boundary condition' outflow boundary condition, Int. J. Numer. Meth. Fluids, 24 (1997), 393-411.
[12] N. K. Ghaddar, G. E. Karniadakis and A. T. Patera, A conservative isoparametric spectral element method for forced convection; Application to fully developed flow in periodic geometries, Numer. Heat Transfer, 9 (1986), 277-300.
[13] J. L. Guermond, P. Minev and J. Shen, Error analysis of pressure-correction schemes for the time-dependent Stokes equations with open boundary conditions, SIAM J. Numer. Anal., 43 (2005), 239-258.
[14] J. L. Guermond and J. Shen, On the error estimates for the rotational pressure-correction projection methods, Math. Comput., 73 (2004), 1719-1737.
[15] F. H. Huang and C. J. Xu, On the error estimates for the rotational pressure-correction projection spectral methods for the unsteady Stokes equations, J. Comput. Math., 23(3) (2005), 285-304.
[16] B. C. V. Johansson, Boundary conditions for open boundaries for the boundaries for the incompressible Navier-Stokes equations, J. Comput. Phys., 105 (1993), 233-251.
[17] M. H. Kobayashi, J. C. F. Pereira and J. M. M. Sousa, Comparison of several open boundary numerical treatments for laminar recirculating flows, Int. J. Numer. Meth. Fluids, 16 (1993), 403-419.
[18] A. G. Kravchenko and P. Moin, Numerical studies of flow over a circular cylinder at Re_D = 3900, Phys. Fluids, 12(2) (2000), 403-417.
[19] Y. M. Lin and C. J. Xu, A fractional step method for the unsteady viscous/inviscid coupled equations, in: Y. Lu, W. Sun and T. Tang (Eds.), Advances in Scientific Computing and Applications, Science Press, Beijing/New York, 2004, pp. 286-294.
[20] J. M. Luijkx, J. K. Platten and J. C. Legros, On the existence of thermoconvective rolls, transverse to a superimposed mean Poiseuille flow, Int. J. Heat Mass Tran., 24 (1981), 803-817.
[21] Y. Maday, D. Meiron, A. T. Patera and E. M. Ronquist, Analysis of iterative methods for the steady and unsteady Stokes problem: Application to spectral element discretization, SIAM J. Sci. Comput., 14(2) (1993), 310-337.
[22] Y. Maday and A. T. Patera, Spectral element methods for the Navier-Stokes equations, in: A. K. Noor (Ed.), State-of-the-Art Surveys in Computational Machanics, ASME, New York, 1988, pp. 71-143.
[23] Y. Maday, A. T. Patera and E. M. Ronquist, An operator integration-factor splitting method for time-dependent problems: Application to incompressible fluid flow, J. Sci. Comput., 5 (1990), 263-292.
[24] S. Mittal, Computation of three-dimensional flows past circular cylinder of low aspect ratio, Phys. Fluids, 13(1) (2001), 177-191.
[25] J. Nordstrom, Accurate solutions of the Navier-Stokes equations despite unknown outflow boundary data, J. Comput. Phys., 120 (1995), 184-205.
[26] X. Nicolas, P. Traore, A. Mojtabi and J. P. Caltagirone, Augmented Lagrangian method and open boundary conditions in 2D simulation of Poiseuille-Bénard channel flow, Int. J. Numer. Meth. Fluids, 25 (1997), 265-283.

[27] I. Orlanski, A simple boundary condition for unbounded hyperbolic flows, J. Comput. Phys., 21 (1976), 251-269.
[28] M. T. Ouazzani, J. P. Caltagirone, G. Meyer and A. Mojtabi, Etude numérique et expérimentale de la convection mixte entre deux plans horizontaux à températures différentes, Int. J. Heat Mass Tran., 32 (1989), 261-269.
[29] S. A. Orszag, M. Israeli and M. O. Deville, Boundary condition for incompressible flows, J. Sci. Comput., 1 (1986), 75-111.
[30] M. T. Ouazzani, J. K. Platten and A. Mojtabi, Etude expérimentale de la convection mixte entre deux plans horizontaux à températures différentes–2, Int. J. Heat Mass Tran., 33 (1990), 1417-1427.
[31] R. Pasquetti and C. J. Xu, High-order algorithms for large-eddy simulation of incompressible flows, J. Sci. Comput., 17(1-3) (2002), 297-309.
[32] A. T. Patera, A Spectral element method for fluid dynamics; laminar flow in a channel expansion, J. Comput. Phys., 54 (1984), 468-488.
[33] J. B. Perot, An analysis of the fractional step method, J. Comput. Phys., 108 (1993), 51-58.
[34] T. C. Papanastasiou, M. Malamataris and K. Ellwood, A new outflow boundary condition, Int. J. Numer. Meth. Fluids, 14 (1992), 587-608.
[35] E. Schroder and K. Buhler, Three-dimensional convection in rectangular domains with horizontal throughflow, Int. J. Heat Mass Tran., 38 (1995), 1249-1259.
[36] R. L. Sani and P. M. Gresho, Résumé and remarks on the open boundary condition minisymposium, Int. J. Numer. Meth. Fluids, 18 (1994), 983-1008.
[37] Y. Sun, Z. J. Wang and Y. Liu, High-order multidomain spectral difference method for the Navier-Stokes equations on unstructured hexahedral grids, Commun. Comput. Phys., 2 (2007), 310-333.
[38] C. H. K. Williamson, Vortex dynamics in the cylinder wake, Annu. Rev. Fluid Mech., 28 (1996), 477-539.
[39] C. J. Xu and Y. M. Lin, Open boundary conditions for the spectral simulation of Poiseuille-Bénard flow, Acta Mech. Sinica, 32(1) (2000), 1-10, (in Chinese).
[40] C. J. Xu and Y. M. Lin, Analysis of iterative methods for the viscous/inviscid coupled problem via a spectral element approximation, Int. J. Numer. Meth. Fluids, 32 (2000), 619-646.
[41] C. J. Xu and R. Pasquetti, On the efficiency of semi-implicit and semi-Lagrangian spectral methods for the calculation of incompressible flows, Int. J. Numer. Meth. Fluids, 35 (2001), 319-340.
[42] M. M. Zdravkovich, Flow Around Circular Cylinders, Oxford University Press, New York, 1997.